Ultramicroscopy 179 (2017) 47–56

Contents lists available at ScienceDirect

Ultramicroscopy

journal homepage: www.elsevier.com/locate/ultramic

Compressed sensing for STEM tomography

Laurène Donati[a,1,*], Masih Nilchian[a,1], Sylvain Trépout[b,c,d,e], Cédric Messaoudi[b,c,d,e], Sergio Marco[b,c,d,e], Michael Unser[a]

[a] Biomedical Imaging Group, École polytechnique fédérale de Lausanne, CH-1015 Lausanne, Switzerland
[b] INSERM, U1196, Orsay F-91405, France
[c] Institut Curie, Centre de Recherche, Orsay F-91405, France
[d] CNRS, UMR9187, Orsay F-91405, France
[e] Université Paris-Sud, Orsay F-91405, France

ARTICLE INFO

Article history:
Received 29 June 2016
Revised 28 March 2017
Accepted 4 April 2017
Available online 6 April 2017

Keywords:
STEM
Electron tomography
Image reconstruction
Random-beam scanning
RB-STEM
Compressed sensing

ABSTRACT

A central challenge in scanning transmission electron microscopy (STEM) is to reduce the electron radiation dosage required for accurate imaging of 3D biological nano-structures. Methods that permit tomographic reconstruction from a reduced number of STEM acquisitions without introducing significant degradation in the final volume are thus of particular importance. In random-beam STEM (RB-STEM), the projection measurements are acquired by randomly scanning a subset of pixels at every tilt view. In this work, we present a tailored RB-STEM acquisition-reconstruction framework that fully exploits the compressed sensing principles. We first demonstrate that RB-STEM acquisition fulfills the "incoherence" condition when the image is expressed in terms of wavelets. We then propose a regularized tomographic reconstruction framework to recover volumes from RB-STEM measurements. We demonstrate through simulations on synthetic and real projection measurements that the proposed framework reconstructs high-quality volumes from strongly downsampled RB-STEM data and outperforms existing techniques at doing so. This application of compressed sensing principles to STEM paves the way for a practical implementation of RB-STEM and opens new perspectives for high-quality reconstructions in STEM tomography.

1. Introduction

Electron microscopy (EM) is a powerful imaging modality that has been intensively used over the past decades to study molecular and cellular biology at the nanometer scale [1]. EM exploits the wave-like behavior of electrons in a vacuum and their extremely short wavelength to produce a visualization of biological nano-structures. Several EM variants exist, such as scanning electron microscopy (SEM) [2], transmission electron microscopy (TEM) [3], or their combined version, scanning transmission electron microscopy (STEM) [4]. In bright-field STEM, the electron-transparent specimen is rastered by a focused electron beam and the transmitted radiation is detected. STEM can offer advantages over conventional TEM tomography for thick samples imaging, including a better signal-to-noise ratio (SNR) and improved contrast [5–7]. STEM has recently been applied to the 3D imaging of fully hydrated, vitrified biological specimens (cryo-STEM), yielding improved resolving power and broadening the scope of acceptable biological specimens [8].

Yet, despite its promise, cryo-STEM is subject to the same experimental limitation as other EM techniques — high-resolution imaging requires dense sampling with large electron radiation dosage, yet biological samples are extremely sensitive to electron-induced irradiation damages. This dosage constraint is even more critical in electron tomography (ET), which requires a series of projection images to be taken covering a large range of tilt angles [9]. Moreover, the geometry of conventional tomographic STEM imaging systems constrains the imaging of samples to a limited angular range. As a result, artifacts consequent to a missing wedge of information in the Fourier space may appear on the reconstructed image if the angular coverage is insufficient [10]. A trade-off between the reconstruction quality (*i.e.*, wide and numerous high-SNR acquisitions) and the sample integrity (*i.e.*, low electron dosage) must thus be considered when optimizing 3D STEM imaging.

Several researches have therefore focused on reconstruction methods that address the limited-angle problem and permit lower-

* Corresponding author.
E-mail address: laurene.donati@epfl.ch (L. Donati).
[1] Both authors contributed equally to this work.

http://dx.doi.org/10.1016/j.ultramic.2017.04.003

dose STEM tomographic acquisitions without introducing significant degradation in the final image. These methods can be categorized according to whether the dosage reduction is achieved by angular or spatial downsampling [11].

Tilt-downsampling (T-DS) techniques rely on algorithms that reconstruct a tomographic image from a reduced number of angular views. T-DS is generally performed by acquiring fewer tilt images over the widest possible angular range. To compensate for the induced lack of information, a standard approach is to incorporate prior knowledge in the reconstruction process. Advanced T-DS reconstruction algorithms primarily include discrete algebraic reconstruction techniques (DART) [12,13] and compressing sensing (CS) based approaches [14–17].

Instead of reducing the number of tilt views, image-downsampling (I-DS) techniques reduce the electron beam coverage of individual tilt images. This can be achieved by decreasing the frame size, the per-pixel dwell time, or the beam current density [18]. Alternatively, one can scan only a fraction of the image pixels following a certain downsampling pattern. The recovery of randomly downsampled EM images has notably been the topic of several recent publications. Anderson et al. [19] reconstructed randomly undersampled SEM data by compressed sensing inversion using image smoothness as a prior. For STEM imaging, Stevens et al. [20] applied a Bayesian dictionary-learning technique to restore randomly undersampled STEM measurements, while Saghi et al. [11] used total variation (TV) to inpaint I-DS images, which were then used as input to compressed sensing tomographic reconstruction. To the best of our knowledge, compressed sensing tomographic reconstruction directly using random I-DS STEM data has not yet been demonstrated. As we further explain in this paper, the main difficulty in doing relies on the fact that it is not obvious *a priori* that random undersampling of STEM measurements associated with the classical representation bases fulfills the incoherence condition required by the CS theory.

The recent work by Saghi et al. [11] simulated both T-DS and random I-DS conditions in STEM to demonstrate the feasibility of further reducing the electron dosage by combining both downsampling techniques. The reconstruction was performed in two successive steps. The I-DS tilt images were first filled in by applying TV-inpainting. A volume was then reconstructed from the restored projection measurements using an iterative algorithm with TV-regularization. Again, as far as we know, compressed sensing has not yet been applied to the global tomographic reconstruction of combined T-DS and random I-DS STEM measurements.

In summary, compressed sensing could be a very powerful tool for minimizing the electron dosage in tomographic STEM imaging; however, its potential in this regard has not been fully exploited yet. In this paper, we address the remaining gaps by fully applying the principles of compressed sensing to tomographic STEM. In particular, we demonstrate that random-beam scanning for STEM (RB-STEM) associated with a wavelet representation basis fulfills the incoherence condition required by the CS theory. We then present a regularized tomographic reconstruction framework that reconstructs high-quality volumes from strongly downsampled RB-STEM data. We demonstrate through simulations on synthetic and real projection measurements that the proposed framework outperforms existing techniques at doing so.

The paper is organized as follows. In Section 2, we recall the principles of compressed sensing and three of its key components: sparsity, incoherence and recovery. The applicability and relevance of these principles in the context of tomographic STEM imaging are then demonstrated in the following three sections. Section 3 discusses the sparsity of biological STEM data, Section 4 demonstrates the incoherence of the RB-STEM acquisition scheme, and Section 5 describes the proposed reconstruction framework for incoherent RB-STEM data-sets. The reconstruction framework is evaluated in Section 6. Our conclusions are presented in Section 7.

2. Compressed sensing theory

Compressed sensing (CS) is a powerful mathematical concept for acquiring sparse signals with a minimum number of measurements provided that proper recovery methods are used [21]. CS theory is extremely relevant to biomedical imaging and has recently been applied with great success to multiple imaging modalities [22–25].

In this work, we aim to show that biological specimens with a sparse representation can also be reconstructed from randomly undersampled STEM measurements through an appropriate nonlinear recovery scheme. To set the context, we briefly describe the three central components of CS theory: data sparsity, incoherent sampling and signal recovery. The relevance and applicability of each principle to STEM are analyzed in subsequent sections.

2.1. Sparsity

The theory of compressed sensing relies on the notion of sparsity [21]. A signal is said to be sparse if it has a concise representation in some basis; *i.e.*, if it can be completely represented by few non-zero coefficients when expressed in a proper transform domain. The mathematical formulation is as follows. Let a signal be represented by a vector $\boldsymbol{f} \in \mathbb{R}^N$. Its expansion in an orthonormal $N \times N$ basis $\boldsymbol{\Psi} = [\boldsymbol{\psi}_1 \boldsymbol{\psi}_2 \cdots \boldsymbol{\psi}_N]$ is given by:

$$\boldsymbol{f} = \sum_{n=1}^{N} x_n \boldsymbol{\psi}_n \tag{1}$$

where $\boldsymbol{x} = (x_1, x_2, \ldots, x_N)$ is the sequence of coefficients of $\boldsymbol{f}$, with x_n defined as $x_n = \langle \boldsymbol{f}, \boldsymbol{\psi}_n \rangle$. The implication of sparsity is that, in a sparsifying domain, few of the coefficients x_n are non-null and thus concentrate most of the signal information. The relevance to signal compression then becomes obvious: numerous zero coefficients in a sparse signal can be discarded without introducing any perceptual loss [26]. In practice, most objects of interest are not exactly sparse, but rather "approximately sparse" (*i.e.*, compressible). For these signals, most of the coefficients in the sparsifying domain have near-zero values instead of strictly null ones.

2.2. Incoherent sampling

It is well known in signal processing that sampling a signal below the Nyqvist frequency introduces aliasing artifacts that are manifested by periodizations in the Fourier domain [27]. The key in CS is to use some form of nonuniform sampling scheme to introduce *incoherent* artifacts in the sparsifying transform domain. These artifacts are said to be incoherent because they spread uniformly throughout the representation domain in a noise-like manner. Hence, they can be distinguished from the signal of interest through sparsity-promoting reconstruction, as the few significant signal coefficients stand out from the introduced incoherent interference [21].

The smallest sampling frequency that can accurately capture the signal information is directly determined by the incoherence between the sensing basis and the (sparse) representation basis [28]. Simply said, the less coherence, the fewer the number of samples needed for proper signal reconstruction. Typical examples of low coherence sensing/representation basis pairs in CS notably include the spike/Fourier basis or the wavelets/noiselets basis [29]. Finally, it is important to note that the row vectors of random matrices are largely incoherent with any fixed basis and therefore they can very efficiently capture signal information with minimal number of measurements

2.3. Signal recovery

The performance of the CS approach relies on appropriate non-linear recovery schemes that efficiently reconstruct the signal of interest from the collected data. The transform coefficients $\tilde{\mathbf{x}}$ are reconstructed after sampling by solving the following optimization problem:

$$\tilde{\mathbf{x}} = \min_{\boldsymbol{x}\in\mathbb{R}^N} \left\{ \| \boldsymbol{y} - \boldsymbol{A}\boldsymbol{x}\|_{l_2}^2 + \| \boldsymbol{x}\|_{l_1} \right\}. \tag{2}$$

Here $\boldsymbol{y} \in \mathbb{R}^M$ refers to the measured data, while $\boldsymbol{A}$ is a $M \times N$ matrix incorporating the model of the imaging process and the sparsifying transform. The first term in Eq. (2) enforces data consistency through l_2-norm minimization, while the second term promotes sparsity through l_1-norm minimization. In other words, the minimization of the objective function yields the sparsest solution among all solutions compatible with the measured data [21,31]. Algorithms for solving Eq. (2) notably include projection onto convex sets, iterative fast thresholding, or iterative reweighted least squares [32]. The final image f is reconstructed by computing $\boldsymbol{f} = \sum_{n=1}^{N} \tilde{x}_n \boldsymbol{\psi}_n$.

3. Sparsity of STEM data

It is well established that natural images are compressible in appropriate domains such as the discrete cosine transform (DCT) and discrete wavelet transform (DWT) [26]. Similarly, the compressibility of various signals relevant to biomedical imaging has been demonstrated by multiple researches [22,23,33,34]. In electron microscopy, Anderson et al. [19] assessed the sparsity of typical electron microscopy images (SEM, TEM and E-SEM) in the block-DCT domain. For electron tomography (ET), Song et al. [35] showed that cryo-ET projections exhibit sparsity in the DCT domain. Finally, the suitability of the DWT for sparsely representing ET data has also been demonstrated in a number of empirical studies [36–38]. For the sake of completeness, we illustrate the compressibility of STEM data in the DWT in Fig. 1.

4. Random-beam scanning in STEM

We shall now demonstrate that random-beam scanning in STEM (RB-STEM) associated with the wavelet domain fulfills the incoherence condition required by compressed sensing. As previously explained, this amounts to showing that the artifacts introduced by the measurement process behave in a “noise-like” manner in the representation domain.

In RB-STEM, the measurement process consists of the random scanning of a subset of pixels for every tilt view (*i.e.*, random I-DS). The considered randomized subsampling regime follows a uniform distribution. The scanning corresponds to the straight-line transmission of an electron beam through the sample, as in a conventional STEM set-up (see Fig. 2). As we describe in the Appendix A, this transmission process can be mathematically modeled by the X-ray transform.

4.1. Incoherence analysis

To measure the incoherence between the two aforementioned bases, we use the transform point spread function (TPSF) analysis proposed by Lustig et al. [22]. The TPSF generalizes the notion of point spread function (PSF), as it assesses “how a single transform coefficient of the underlying object ends up influencing other transformed coefficients of the measured undersampled object”.

The results of the incoherence analysis are displayed in Fig. 3. The evaluation is performed on 64×64 synthetic data representing a single square surrounded by zero values (Fig. 3b). A filtered back-projection (FBP) of 1800 angular views (equally-spaced in $[0; 2\pi]$) is used to reconstruct the image (Fig. 3c). FBP has indeed been shown to provide a good approximation of the inverse X-ray transform operator for the reconstruction of $N \times N$ images if at least $\pi \times N$ angles are imaged [39]. A uniform I-DS scheme (Fig. 3d–f) is considered to allow comparison with the random I-DS regime (Fig. 3g–i).

The results demonstrate that the incoherence between the RB-STEM measurement domain and the wavelet domain is more than satisfactory, as the introduced artifacts have a strongly incoherent behaviour in the transform domain (Fig. 3i). In contrast, a structured I-DS scheme leads to a much less suitable outcome (Fig. 3f). Overall, these results validate the application of compressed sensing to RB-STEM and guarantee that the signal of interest may be recovered, assuming that a proper non-linear recovery scheme is used.

5. Reconstruction of incoherent RB-STEM data

The recovery of high-quality images from a limited number of incoherent RB-STEM projection measurements relies strongly on a high-performance reconstruction framework. In this section, we describe the discretization scheme used to formulate the reconstruction problem and the algorithm we developed to solve it.

5.1. Discretization scheme

Tomographic STEM aims at reconstructing a three-dimensional signal f using a given set of STEM measurements $g(\boldsymbol{y}_i, \theta_i)$. Here $(\boldsymbol{y}_i, \theta_i) \in Y \times \Theta$ with $i \in \{1, 2, \cdots, M\}$ where M corresponds to the number of measurements. The set Y contains the different positions of the STEM gun scans on the projection plane, and the set of all tilt angles is collected in Θ.

In order to formulate the reconstruction as an inverse problem, it is necessary to discretize both the signal and the imaging operator. The standard approach is to fix the reconstruction space to functions of the form [27,40]:

$$f(\boldsymbol{x}) = \sum_{\boldsymbol{k}\in\Omega} \mathrm{c}_{\boldsymbol{k}} \varphi(\boldsymbol{x} - \boldsymbol{k}), \tag{3}$$

where $\varphi(\cdot - \mathbf{k}) \in L_2(\mathbb{R}^3)$ with $\boldsymbol{k} = (k_1, k_2, k_3) \in \mathbb{Z}^3$ are appropriate functions, while $\Omega = \{-N_1 \cdots N_1\} \times \{-N_2 \cdots N_2\} \times \{-N_3 \cdots N_3\}$ specifies the support of the object $(N_1, N_2, N_3 \in \mathbb{N})$. The function $f(\boldsymbol{x})$ is described by its coefficients $\mathrm{c}_{\boldsymbol{k}}$. Using the linearity and pseudo-shift-invariance of the X-ray transform [41], we model the effect of the projection operator $\mathcal{P}$ by:

$$\begin{aligned} \mathcal{P} f(\boldsymbol{y}; \theta) &= g(\boldsymbol{y}; \theta) \\ &= \sum_{\boldsymbol{k}\in\Omega} \mathrm{c}_{\boldsymbol{k}} \mathcal{P}\varphi(y_1 - k_1 \cos\theta - k_2 \sin\theta, y_2 - k_3; \theta). \end{aligned} \tag{4}$$

This, in turn, translates into the matrix formulation of the STEM imaging model as

$$\mathbf{g} = \mathbf{H}\,\mathbf{c}, \tag{5}$$

with $\mathbf{g} \in \mathbb{R}^M$ whose ith entry is $[\mathbf{g}]_i = g(\boldsymbol{y}_i, \theta_i)$, and $\mathbf{c} \in \mathbb{R}^N$ a vector representation of the coefficients (3) indexed by $\mathbf{k}$ with $N = (2N_1 + 1)(2N_2 + 1)(2N_3 + 1)$. The entries of the system matrix $\mathbf{H} \in \mathbb{R}^{M\times N}$ are $[\mathbf{H}]_{i,\boldsymbol{k}} = \mathcal{P}\varphi(y_{i,1} - k_1 \cos\theta - k_2 \sin\theta, y_{i,2} - k_3; \theta_i)$, where $[\boldsymbol{y}]_i = (y_{i,1}, y_{i,2})$. In standard STEM, for every tilt angle θ, the whole projection plane is scanned uniformly with $\boldsymbol{y}_i = i\Delta\boldsymbol{y}$ where $i \in \{-M, \cdots, M\}$. The detector resolution is specified by $\Delta\boldsymbol{y} = (\Delta y_1, \Delta y_2)$.

In contrast, the acquired measurements positions $(\boldsymbol{y}_i, \theta_i)$ in RB-STEM are determined by a random scanning pattern $\mathbf{S}$. The set of positions are denoted by $(\boldsymbol{y}_i, \theta_i) \in Y_S \times \Theta_S$ where the elements in the set $Y_S \times \Theta_S$ are specified by the sampling pattern S.

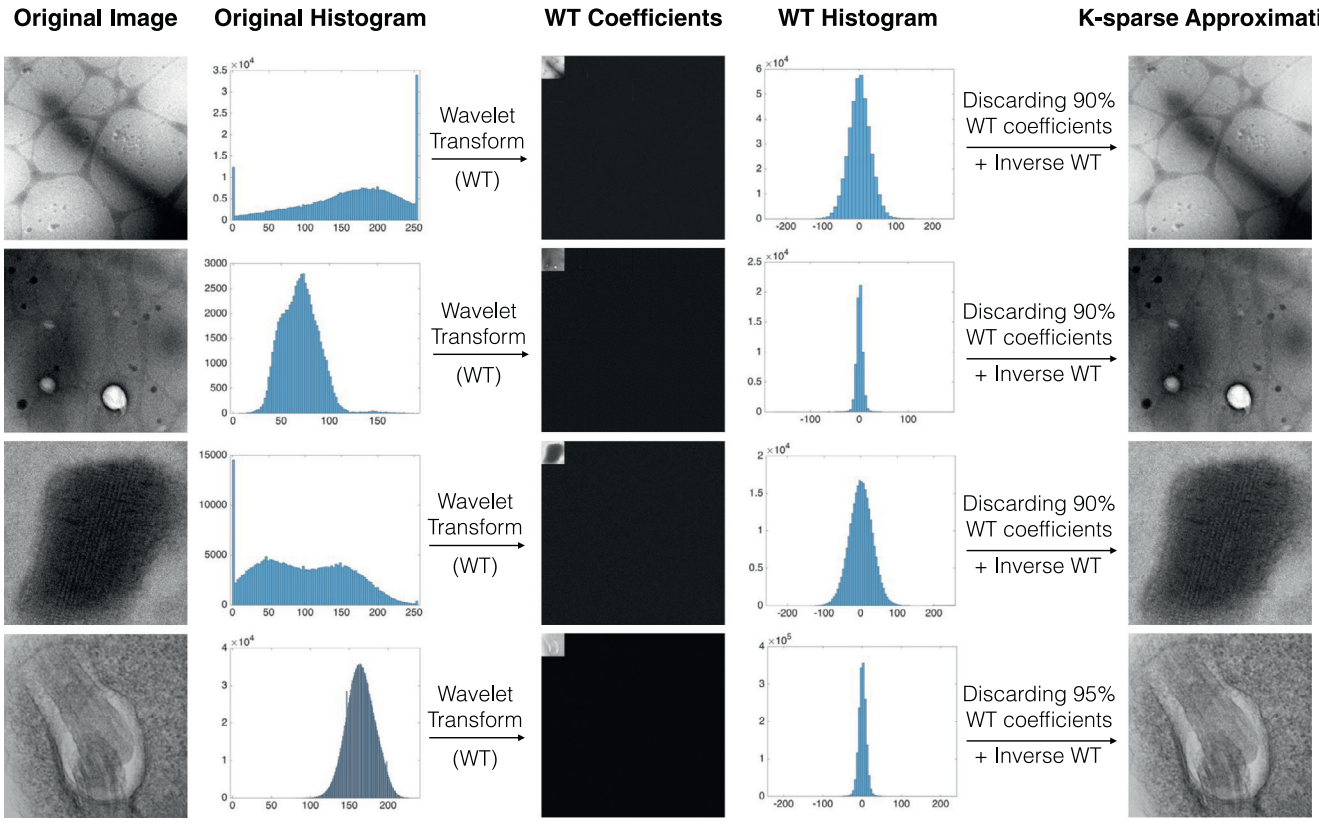

Fig. 1. Illustration of the compressibility of biological STEM samples in the Haar wavelet transform domain. We consider typical STEM samples and compute their Haar wavelet coefficients using the ImageJ software [30]. We then discard most of these coefficients (90%–95%) and compute the inverse transform to get the K-sparse approximation of the original images. In the image domain, a large range of non-zero coefficients is observed for all samples (left histograms). In contrast, most coefficients in the sparsifying domain have near-zero values (right histograms). As a result, discarding of 90%–95% of the transform coefficients does not lead to significant perceptual losses in the inverse-transformed images (far right). This confirms the approximate sparsity of STEM data in the wavelet domain.

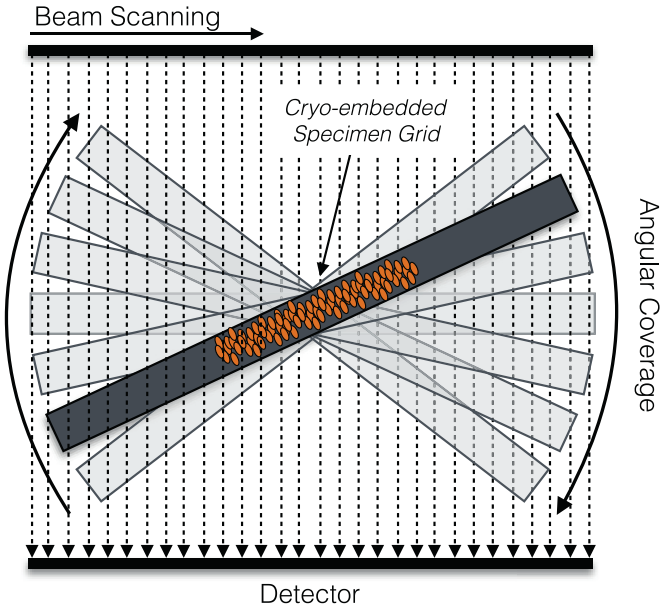

Fig. 2. Illustration of the conventional cryo-STEM acquisition process. Lenses are used to concentrate/focus all the electron flow in a single beam, and the image is then rastered. Different beam scanning patterns may be used to downsample the individual tilt images (I-DS). Downsampling of the number of tilt views (T-DS) is also feasible.

This is equivalent to formulating the RB-STEM imaging process as $\mathbf{g} = \mathbf{S}\mathbf{H}\mathbf{c}$.

5.2. Reconstruction algorithm

We have argued that biological samples in electron tomography are sparse in the wavelet domain. It has been recently demonstrated that sparsity in the Haar wavelet domain ensures sparsity in the gradient domain [42,43]. Consequently, the RB-STEM measurement domain $\mathbf{H}$ is also incoherent with respect to the gradient domain associated to the transform $\mathbf{L}$. Thus, assuming that the number of measurements fulfills the CS requirements, the theory of compressed sensing ensures that we can reconstruct the three-dimensional volume using ℓ_1-minimization [44]:

$$\min_{\mathbf{c}\in\mathbf{R}^n} \|\mathbf{L}\mathbf{c}\|_1 \text{ subject to } \|\mathbf{H}\mathbf{c} - \mathbf{g}\|^2 \leq \epsilon\,. \tag{6}$$

We developed a fast and highly-efficient regularized iterative algorithm to solve this optimization problem. In our implementation we used total-variation (TV) regularization rather than wavelet-based one, as TV has been shown to act in a similar qualitative way while yielding slightly better results [45–47]. The design of the proposed algorithm is further detailed in the Appendix A.

6. Reconstruction results

6.1. Synthetic projection measurements

We shall first demonstrate through simulations on synthetic data the superiority of random I-DS methods over uniform T-DS approaches at various downsampling levels. We then analyse the

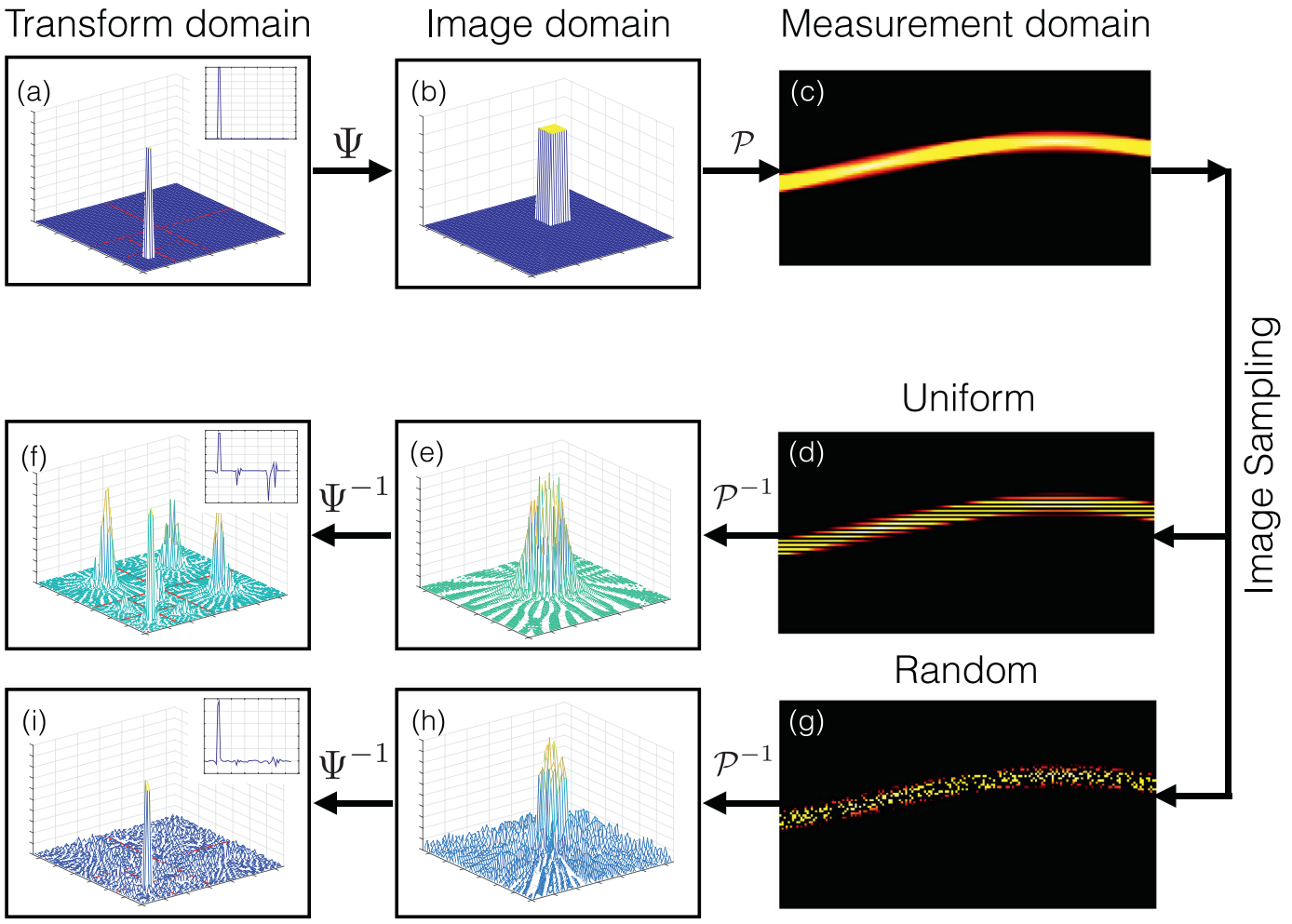

Fig. 3. Comparison of the reconstruction of a sparse signal (top row) from two different downsampling approaches: uniform sinogram sampling (middle row) and random sinogram sampling (bottom row). Projection measurements (*c*) of the spatial signal (*b*) harbor an "impulse-like" sparse expansion (*a*) in the wavelet domain. Uniform undersampling of measurements (*d*) is associated with a transformed point-spread function (TPSF) with coherent aliasing (*f*). In contrast, random undersampling of measurements (*g*) results in incoherently aliased TPSF (*i*). As a corollary, filtered-back projection reconstruction of the randomly sampled measurements (*h*) shows more similarity to the original signal (*b*) than the signal reconstructed from uniform sampling (*e*). The upper-right boxes in (*a*), (*f*), and (*i*) display profile views of the respective sparse representations.

performance of our algorithm at reconstructing 3D volume from 2D synthetic random I-DS projection measurements by comparing it to the existing algorithm.

6.1.1. Simulation conditions

The synthetic volume used as the ground truth in the simulations is a $512 \times 512 \times 256$ visualization of the flagellar pocket of a trypanosome (Fig. 4), acquired as presented in [48]. All simulations were implemented in Matlab (MathWorks, Natick, MA, USA). To simulate the acquisition processes, two variants of the projection operator were coded: one using Kaiser-Bessel window functions (KBWF) as discretizing functions and one using B-splines [49]. To reduce the risk of committing an "inverse crime", the projection operator producing the synthetic measurements always differed from the one used for reconstruction. The tilt-downsampling condition was achieved by uniformly increasing the angular increment between two simulated tilt-series (*i.e.*, uniform T-DS). To mimic the "missing wedge of information" effect, we considered an angular coverage of $(-70°; +70°)$, with a 1° increment (*i.e.*, 140 tilt views). Spatial downsampling in the image domain was achieved by applying a uniformly randomized subsampled binary mask over the simulated projection measurements (*i.e.*, random I-DS).

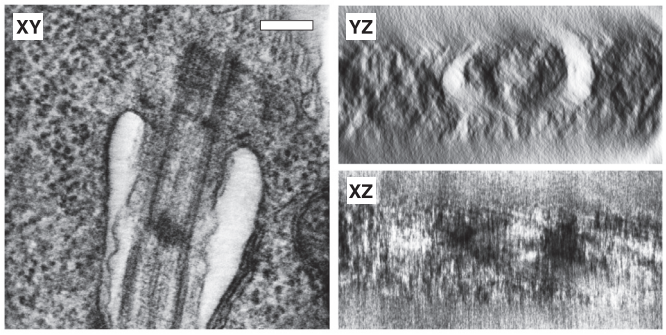

Fig. 4. Orthoslices of the ground truth image depicting the flagellar pocket of a trypanosome. The XY slice shows a typical representation of a flagellar pocket, with the flagella separating the pocket into two sides of different sizes. The YZ orientation shows an orthogonal section of the flagella. In this context, the XZ slice displays microtubule tracks. The scale bar indicates 250 nm.

Our 3D reconstruction task was performed through an in-house code implementing the framework presented in Section 5. Isotropic total-variation (TV) regularization was used to promote sparsity. The optimization of the hyper-parameters (*c.f.* Eq. (8)) was performed by visual assessment.

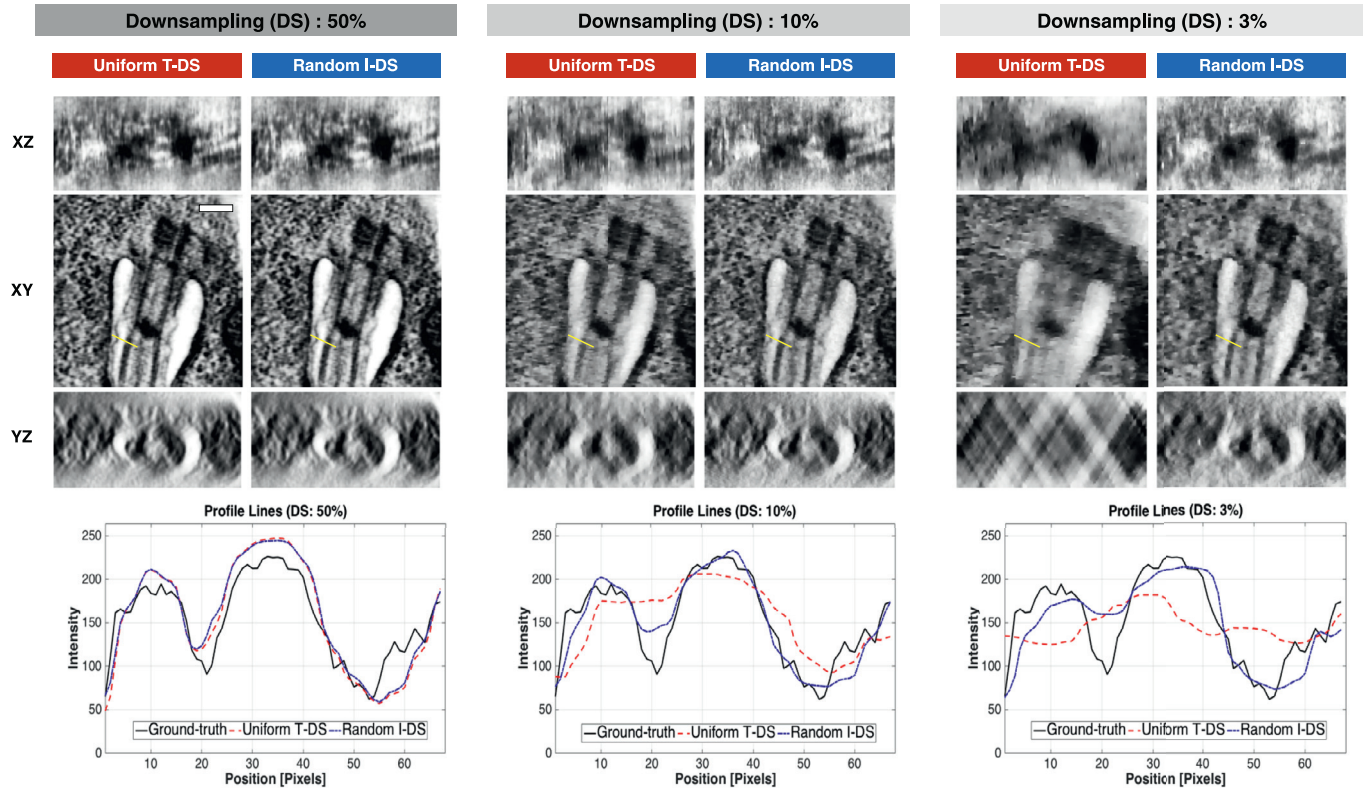

Fig. 5. (Top) Cross-sectional slices through the reconstructed flagellar pocket from uniform T-DS synthetic projection measurements and random I-DS synthetic projection measurements at various downsampling ratios (50%, 10%, 3%). The same reconstruction framework is used to recover all datasets. (Bottom) Profile lines taken on the XY-orthoslices of the reconstructed volumes. The position of the profile line is indicated in yellow on the orthoslices. The scale bar indicates 250 nm. (For interpretation of the references to color in this figure legend, the reader is referred to the web version of this article.)

6.1.2. Comparison with T-DS approach

We first compared the performance of random I-DS approaches over classic T-DS techniques at various electron radiation doses. To do so, we simulated both downsampling conditions on synthetic data and reconstructed the obtained measurements with our algorithm.

Fig. 5 shows orthoslices of the reconstructed volumes when only 50%, 10%, and 3% of the pixels are scanned. High-quality reconstructions are obtained for both frameworks when half of the pixels are scanned. This is confirmed by the clear overlapping of their corresponding profile lines. However, when the ratio of scanned pixels falls below 10%, the reconstructions from the uniform T-DS measurements are strongly degraded whereas those originating from random I-DS acquisitions remain of satisfactory quality. The profile lines on the 3% reconstructions are especially informative on this robustness of the RB-STEM framework. Whereas the T-DS approach fails to retrieve the important changes in intensity, the random I-DS approach still permits to delimit the borders of the main trypanosome structures.

Overall, those results confirm that reconstructing sparse objects from incoherent acquisitions outperforms uniform (tilt)-downsampling approaches, as predicted by the theory of CS and by our TPSF analysis results (see Section 4). To further emphasize the relevance of the proposed RB-STEM acquisition-reconstruction framework, hereafter we refer to random I-DS data as random-beam STEM (RB-STEM) measurements.

6.1.3. Comparison with existing algorithm

We then compared our integrated framework for the reconstruction of RB-STEM measurements to the pioneering approach proposed by Saghi et al. [11]. To the best of our knowledge, there is no other prior work developed in this area. In their paper, the authors propose to perform this tomographic reconstruction task in two steps. First, they fill in the missing data through TV inpainting in order to produce conventional projections. Second, they use an iterative algorithm with TV-regularization for the tomographic reconstruction of the projection views. We have reimplemented their algorithm as described in [11] in order to compare our compressed sensing framework to their approach. The optimization of the hyper-parameters is performed by visual assessment.

Fig. 6 presents orthoslices views of the reconstructions of RB-STEM data achieved by both frameworks at 50% and 20% downsampling ratios (top). The corresponding Fourier shell correlation (FSC) are also displayed (middle), as well as profile lines taken on the XY-orthoslices of the reconstructed volumes (bottom). Visual and quantitative analysis of these results indicate that, at equivalent dose reduction, the proposed RB-STEM reconstruction algorithm outperforms the existing algorithm. Finer details (*e.g.*, filament-like structures) can be visually retrieved from the reconstructions achieved by our framework, at both 50% and 20% downsampling. In addition, both the FSC curves and the profile lines indicate that the proposed framework achieves higher resolution at both sampling levels. Several reasons might be put forward to explain those improvements.

First, the proposed RB-STEM algorithm performs the tomographic reconstruction in a single global fashion, as prescribed by the theory of compressed sensing. Significant advantages follow, such as the fact that combining more data gives more information about the object of interest. Moreover, the influence of sparsity increases with the dimensionality of the reconstruction procedure.

Second, as explained by the authors themselves in their discussion [11], their reliance on an intermediate TV-inpainting step limits their capacity to reconstruct fines structures when only few

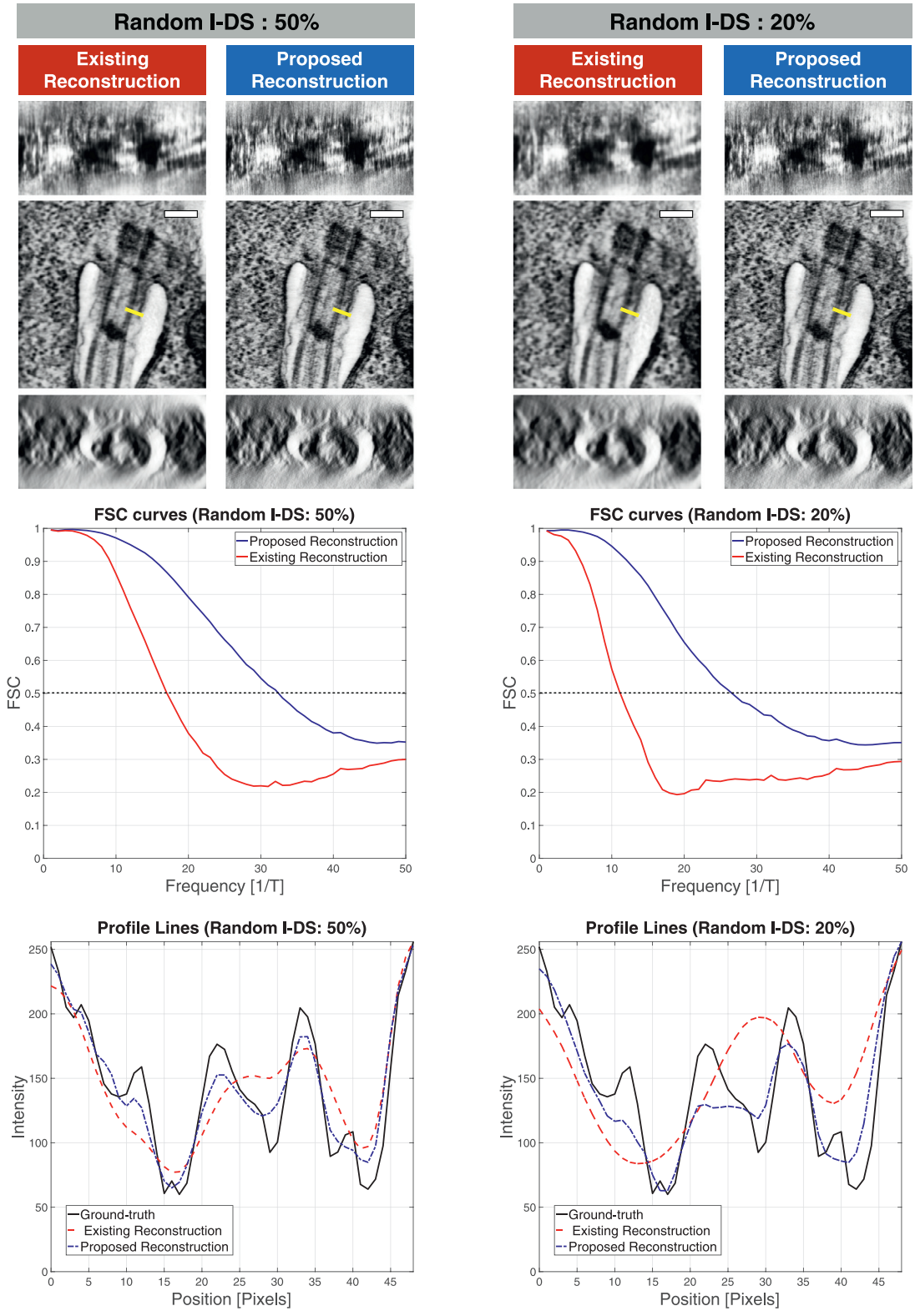

Fig. 6. Comparison of the proposed algorithm with the existing algorithm for the reconstruction of synthetic random I-DS projection measurements of *T. brucei*. (Top) Cross-sectional slices through the reconstructed flagellar pocket for both algorithms at 50% and 20% downsampling. (Middle) FSC curves of the reconstructed volumes for both algorithms at 50% and 20% downsampling. The FSC curve provides a measure of resolution by comparing the Fourier transforms of the ground truth volume and of the reconstructed volume at different frequencies. The spatial frequency at which the FSC curve falls below a certain FSC criterion (commonly fixed at FSC = 0.5 in the community) indicates the achieved resolution. (Bottom) Profile lines taken on the XY-orthoslices of the reconstructed volumes. The position of the profile line is indicated in yellow on the orthoslices. The scale bars indicate 250 nm. (For interpretation of the references to color in this figure legend, the reader is referred to the web version of this article.)

pixels are scanned. The primary limitation is that performing TV-inpainting on heavily downsampled measurements tends to introduce strong staircase artifacts in the restored images. By contrast, our framework performs the reconstruction directly from the downsampled measurements. Thus, it is not limited by the morphology nor by the fineness of the structures to be imaged. This translates into reconstructions of highly-detailed specimens that are globally more robust to the electron dosage reduction.

Our approach also simplifies the optimization procedure, as it only requires the optimization of a single hyper-parameter. In addition, this parameter has demonstrated good stability in regard to the downsampling ratios. This stability is a significant advantage, as it promotes consistency in the reconstructions while greatly shortening the optimization procedure.

6.2. Real projection measurements

To get insight on the robustness of the RB-STEM reconstruction framework in real conditions, we created RB-STEM datasets by simulating random I-DS on *real* STEM projection measurements. The difference with the previous experiment is important, as the use of real STEM projection measurements and the presence of noise increases the ill-posedness of the reconstruction problem.

6.2.1. Sample preparation

T. brucei cells were cultured in SDM79 medium supplemented with haemin and 10% foetal calf serum, as described in [50]. *T. brucei* cells were fixed directly in the culture flask with 2.5% glutaraldehyde and 4% PFA for 30 min at room temperature. Cells were rinsed three times in PBS and subsequently post-fixed in 1% OsO_4 for 30 min at room temperature. Cells were dehydrated in baths of increasing ethanol concentrations at 4 °C and included in Epon resin. Sections of 500 nm were prepared using an ultramicrotome and were mounted on electron microscopy copper grids for observation.

6.2.2. Data acquisition

Tomographic tilt-series were acquired using the bright-field STEM detector (camera length: 60 cm; magnification: 150,000; probe size: 1.5 nm; convergence semi-angle of the beam: 25 mrad; collection semi-angle of the detector: 6.667 mrad) on a JEOL 2200FS field emission gun 200 kV electron microscope (JEOL© Ltd.). A total of 100 tilt views were acquired following a Saxton scheme [51] from $-70°$ up to $+70°$ with tilt increments varying between 1° (at the highest tilt angles) and 2° (at the lowest tilt angles around 0°). Images were recorded using the Recorder software (JEOL© Ltd.). A total of five images with different foci were collected for each tilt angle and merged as described in [48], enabling the recovery of information at focus through the whole sample depth.

6.2.3. Simulations and reconstructions

To mimic the RB-STEM process, we randomly downsampled the real projection measurements by applying a uniformly randomized subsampled binary mask. The reconstruction is performed as described in Section 6.1.1.

Fig. 7 compares the $512 \times 512 \times 256$ reconstruction from a complete STEM dataset (*i.e.*, no I-DS) with the same-sized reconstruction obtained when only 30% of the projection measurements are scanned following a random I-DS scheme.

The results show that even when only a third of the real projection measurements is retained, the reconstruction still achieves to preserve key information about the main structures of the imaged biological sample. In particular, all the annotated structures in Fig. 7 can still be located and distinguished from one another

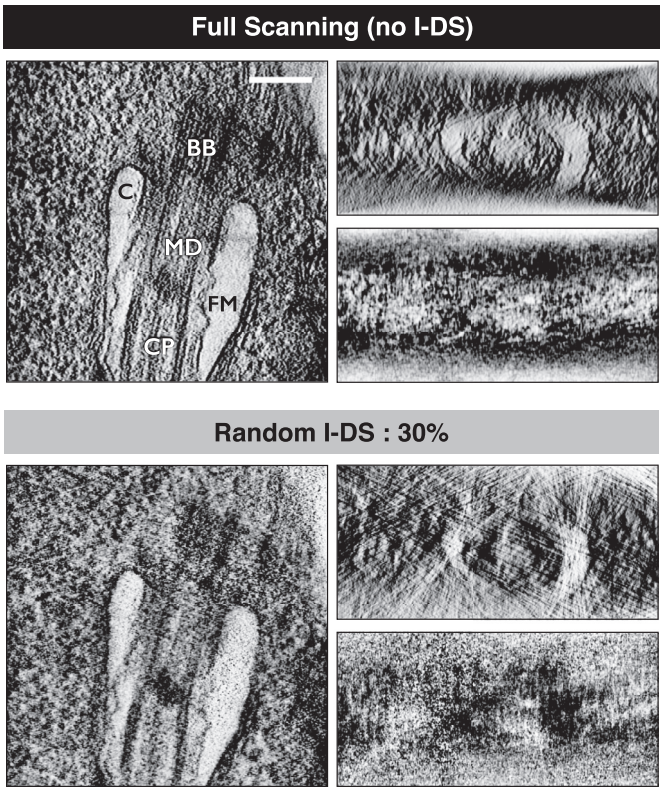

Fig. 7. Cross-sectional slices through the reconstructed flagellar pocket of *T. brucei* from real STEM projection measurements with no simulated random I-DS (top) or with 30% random I-DS (bottom). The indicated biological structures are the basal body (BB), the collarette (C), the central pair (CP), the flagellar membrane (FM) and the microtubules doublets (MD). The scale bar indicates 250 nm.

in the RB-STEM reconstruction (Fig. 7-bottom). Moreover, the contours of the collarette and the flagellar membrane are correctly recovered. The analysis of the central structures of the flagellar pocket (*i.e.*, the basal body, the microtubules doublets and the central pair) underlines the difficulty of recovering the higher-frequency details. Nevertheless, visual information on the shapes and textures of those structures can be retrieved from the reconstructed RB-STEM volume.

Along with the aforementioned experiments, those results tend to confirm the robustness of the RB-STEM reconstruction framework in presence of noise and with reduced information.

7. Conclusion

We developed a regularized tomographic reconstruction framework to recover high-quality volumes from randomly downsampled STEM projection measurements (*i.e.*, RB-STEM data). This acquisition-reconstruction framework was built upon the demonstration that, in contrast to uniform downsampling methods, RB-STEM fulfills the “incoherence” condition required by the compressed sensing theory. Its superiority over tilt-downsampling approaches was then demonstrated through simulations on synthetic RB-STEM data. We also showed that the proposed algorithm outperforms the existing approach for the reconstruction of randomly downsampled STEM measurements.

Overall, this work establishes the potential of RB-STEM to produce quality reconstructions of highly detailed objects imaged at a low electron dose. The development of RB-STEM could thus enable the study of electron-sensitive samples such as cryo-fixed biological samples through less electron-intensive methods. By occurring at a timepoint where cryo-STEM studies are emerging [8],

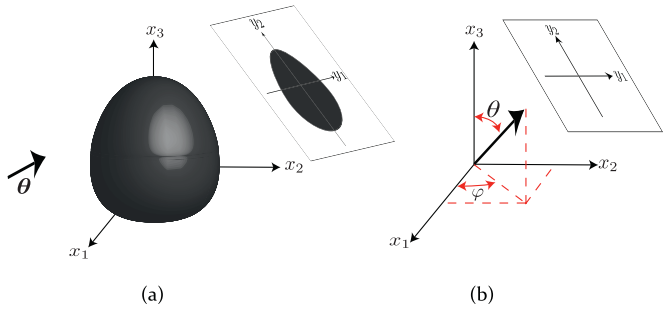

Fig. 8. 3D geometry of the X-ray transform model.

this work could contribute to the feasibility and popularisation of RB-STEM in biological sciences.

Acknowledgments

The authors acknowledge the PICT-IBiSA for providing access to their chemical imaging equipment. The work of L. Donati and M. Nilchian was supported by an ERC grant (ERC-692726-GlobalBioIm). The work of S. Trépout was funded by an ANR grant (ANR-11-BSV8-016).

Appendix A

A1. Image formation model in ET

Due to their extremely short wavelength, electrons approximately travel in straight lines through a sample. Hence, the imaging operator of STEM can be mathematically described through the X-ray transform [41]. The X-ray transform $\mathcal{P}: L_2(\mathbb{R}^3) \to L_2(\mathbb{R}^2 \times [0,\pi))$ maps a 3D function $f(\boldsymbol{x})$ into its 2D line-integral images along different tilt angles:

$$\mathcal{P}\{f(\boldsymbol{x})\}(\boldsymbol{y};\theta) = \int_{\mathbb{R}^3} f(\boldsymbol{x})\delta(y_1 - x_1\cos\theta - x_2\sin\theta, y_2 - x_3)\mathrm{d}\boldsymbol{x}, \tag{7}$$

with $\theta \in [0, \pi)$ and where $\boldsymbol{x} = (x_1, x_2, x_3)$ and $\boldsymbol{y} = (y_1, y_2)$ specify the object and projection coordinates, respectively. Here $\delta(\mathbf{x})$ denotes the two-dimensional delta function. The geometry of the problem is illustrated in Fig. 8.

According to Beer's law and using the X-ray transform, the mathematical model of STEM is defined as

$$g(\boldsymbol{y},\theta) = \log\left(\frac{I(\boldsymbol{y},\theta)}{I_0(\boldsymbol{y},\theta)}\right) = \mathcal{P}f(\boldsymbol{y},\theta),$$

where $I(\boldsymbol{y}, \theta)$ is the intensity acquired by the detector, $I_0(\boldsymbol{y}, \theta)$ is the intensity of the transmitted beam, and θ the tilt angle measured with respect to axis x_1 on the x_1x_2 plane.

A2. Reconstruction algorithm

The reconstruction of a three-dimensional volume from RB-STEM data is a strongly ill-posed problem. CS theory asserts that one can solve this problem through ℓ_1-minimization. The matrix formulation is given in Eq. (6).

The equivalent Lagrange formulation of the optimization is

$$\mathcal{J}(\mathbf{c}) = \min_{\mathbf{c}\in\mathbf{R}^n}\left\{\frac{1}{2}\|\mathbf{H}\mathbf{c} - \mathbf{g}\|^2 + \lambda\|\mathbf{L}\mathbf{c}\|_1\right\}, \tag{8}$$

where λ is an hyper-parameter of the optimization problem. To solve Eq. (8), one can define an auxiliary variable $\mathbf{u} = \mathbf{L}\mathbf{c}$, and rewrite the optimization problem as a constrained optimization problem [52,53],

$$\mathcal{J}(\mathbf{c}) = \min_{\mathbf{c}\in\mathbf{R}^n, \mathbf{u}=\mathbf{L}\mathbf{c}}\left\{\frac{1}{2}\|\mathbf{H}\mathbf{c} - \mathbf{g}\|^2 + \lambda\|\mathbf{u}\|_1\right\}. \tag{9}$$

Its scaled augmented Lagrangian functional can be written in the form of

$$\mathcal{L}_\mu(\mathbf{c},\mathbf{u},\mathbf{d}) = \frac{1}{2}\|\mathbf{H}\mathbf{c} - \mathbf{g}\|^2 + \lambda\|\mathbf{u}\|_1 + \frac{\mu}{2}\|\mathbf{u} - \mathbf{L}\mathbf{c} + \mathbf{d}\|^2. \tag{10}$$

where $\mathbf{d}$ is the Lagrange variable. We use the alternating direction method of multipliers (ADMM) to decompose the optimization problem into a set of simpler ones [52,53],

$$\begin{cases} \mathbf{c}^{k+1} \leftarrow \underset{\mathbf{c}}{\operatorname{argmin}}\ \mathcal{L}_\mu(\mathbf{c},\mathbf{u}^k,\mathbf{d}^k) & (a) \\ \mathbf{u}^{k+1} \leftarrow \underset{\mathbf{u}}{\operatorname{argmin}}\ \mathcal{L}_\mu(\mathbf{c}^{k+1},\mathbf{u},\mathbf{d}^k) & (b) \\ \mathbf{d}^{k+1} \leftarrow \mathbf{d}^k + \mu(\mathbf{L}\mathbf{c}^{k+1} - \mathbf{u}^{k+1}) & (c). \end{cases} \tag{11}$$

Eq. (11)(a) is a quadratic minimization with respect to $\mathbf{c}$,

$$\mathcal{J}_1(\mathbf{c}) = \frac{1}{2}\|\mathbf{H}\mathbf{c} - \mathbf{g}\|^2 + \frac{\mu}{2}\|\mathbf{u} - \mathbf{L}\mathbf{c} + \mathbf{d}\|^2 \tag{12}$$

whose gradient is

$$\nabla\mathcal{J}_1(\mathbf{c}) = \left(\mathbf{H}^\top\mathbf{H} + \mu\mathbf{L}^\top\mathbf{L}\right)\mathbf{c} - \left(\mathbf{H}^\top\mathbf{g} + \mu\mathbf{L}^\top(\mathbf{u} + \mathbf{d})\right). \tag{13}$$

The critical point of the cost functional is the root of the gradient function,

$$\mathbf{c} = \left(\mathbf{H}^\top\mathbf{H} + \mu\mathbf{L}^\top\mathbf{L}\right)^{-1}\left(\mathbf{H}^\top\mathbf{g} + \mu\mathbf{L}^\top(\mathbf{u} + \mathbf{d})\right). \tag{14}$$

Unfortunately, the matrix $\left(\mathbf{H}^\top\mathbf{H} + \mu\mathbf{L}^\top\mathbf{L}\right)$ is not invertible in the case of RB-STEM. We therefore use conjugate gradient to minimize it.

The solution of Eq. (11)(b) is a simple point-wise soft-thresholding operator,

$$\mathbf{u}^{k+1} = \operatorname{prox}_{\frac{\lambda}{\mu}}(\mathbf{L}\mathbf{c}^{k+1} - \mathbf{d}^k). \tag{15}$$

Finally, the last step, Eq. (11)(c) corresponds, to an update of the Lagrange parameter.

References

[1] L.F. Kourkoutis, J.M. Plitzko, W. Baumeister, Electron microscopy of biological materials at the nanometer scale, Annu. Rev. Mater. Res. 42 (1) (2012) 33–58.
[2] M.A. Hayat, Principles and techniques of scanning electron microscopy. biological applications. volume 1., 1974.
[3] D.B. Williams, C.B. Carter, The transmission electron microscope, in: Transm. Electron Microsc., Springer US, Boston, MA, 1996, pp. 3–17.
[4] S.J. Pennycook, P.D. Nellist (Eds.), Scanning transmission electron microscopy, Springer New York, New York, NY, 2011.
[5] M.F. Hohmann-Marriott, A.A. Sousa, A.A. Azari, S. Glushakova, G. Zhang, J. Zimmerberg, R.D. Leapman, Nanoscale 3D cellular imaging by axial scanning transmission electron tomography, Nat. Methods 6 (10) (2009) 729–731.
[6] K. Aoyama, T. Takagi, A. Hirase, A. Miyazawa, STEM tomography for thick biological specimens, Ultramicroscopy 109 (1) (2008) 70–80.
[7] A. Yakushevska, M. Lebbink, W. Geerts, L. Spek, E. van Donselaar, K. Jansen, B. Humbel, J. Post, A. Verkleij, A. Koster, STEM tomography in cell biology, J. Struct. Biol. 159 (3) (2007) 381–391.
[8] S.G. Wolf, L. Houben, M. Elbaum, Cryo-scanning transmission electron tomography of vitrified cells, Nat. Methods 11 (4) (2014) 423–428.
[9] J. Frank (Ed.), Electron Tomography: Methods for Three-Dimensional Visualization of Structures in the Cell, Springer New York, New York, NY, 2006.
[10] N. Kawase, M. Kato, H. Nishioka, H. Jinnai, Transmission electron microtomography without the missing wedge for quantitative structural analysis, Ultramicroscopy 107 (1) (2007) 8–15.
[11] Z. Saghi, M. Benning, R. Leary, M. Macias-Montero, A. Borras, P.A. Midgley, Reduced-dose and high-speed acquisition strategies for multi-dimensional electron microscopy, Adv. Struct. Chem. Imaging 1 (1) (2015) 7.
[12] K. Batenburg, S. Bals, J. Sijbers, C. Kübel, P. Midgley, J. Hernandez, U. Kaiser, E. Encina, E. Coronado, G. Van Tendeloo, 3D imaging of nanomaterials by discrete tomography, Ultramicroscopy 109 (6) (2009) 730–740.
[13] S. Van Aert, K.J. Batenburg, M.D. Rossell, R. Erni, G. Van Tendeloo, Three-dimensional atomic imaging of crystalline nanoparticles, Nature 470 (7334) (2011) 374–377.
[14] R. Leary, Z. Saghi, P.A. Midgley, D.J. Holland, Compressed sensing electron tomography, Ultramicroscopy 131 (2013) 70–91.

[15] Z. Saghi, D.J. Holland, R. Leary, A. Falqui, G. Bertoni, A.J. Sederman, L.F. Gladden, P.A. Midgley, Three-dimensional morphology of iron oxide nanoparticles with reactive concave surfaces. a compressed sensing-electron tomography (CS-ET) approach, Nano Lett. 11 (11) (2011) 4666–4673.
[16] O. Nicoletti, F. de la Peña, R.K. Leary, D.J. Holland, C. Ducati, P.A. Midgley, Three-dimensional imaging of localized surface plasmon resonances of metal nanoparticles, Nature 502 (7469) (2013) 80–84.
[17] B. Goris, S. Bals, W. Van den Broek, E. Carbó-Argibay, S. Gómez-Graña, L.M. Liz–Marzán, G. Van Tendeloo, Atomic-scale determination of surface facets in gold nanorods, Nat. Mater. 11 (11) (2012) 930–935.
[18] J.P. Buban, Q. Ramasse, B. Gipson, N.D. Browning, H. Stahlberg, High-resolution low-dose scanning transmission electron microscopy., J. Electron Microsc. (Tokyo). 59 (2) (2010) 103–112.
[19] H.S. Anderson, J. Ilic-Helms, B. Rohrer, J. Wheeler, K. Larson, Sparse imaging for fast electron microscopy, Proc. SPIE-IS&T Electron. Imaging 8657 (2013) 86570C.
[20] A. Stevens, H. Yang, L. Carin, I. Arslan, N.D. Browning, The potential for bayesian compressive sensing to significantly reduce electron dose in high-resolution STEM images, Microscopy 63 (1) (2014) 41–51.
[21] E. Candes, M. Wakin, An introduction to compressive sampling, IEEE Signal Process. Mag. 25 (2) (2008) 21–30.
[22] M. Lustig, D. Donoho, J.M. Pauly, Sparse MRI: the application of compressed sensing for rapid MR imaging., Magn. Reson. Med. 58 (6) (2007). 1182–95.
[23] L. Zhu, W. Zhang, D. Elnatan, B. Huang, Faster STORM using compressed sensing, Nat. Methods 9 (7) (2012) 721–723.
[24] R.M. Willett, R.F. Marcia, J.M. Nichols, Compressed sensing for practical optical imaging systems: a tutorial, Opt. Eng. 50 (7) (2011) 072601–072601–13.
[25] A. Pacureanu, M. Langer, E. Boller, P. Tafforeau, F. Peyrin, Nanoscale imaging of the bone cell network with synchrotron x-ray tomography: optimization of acquisition setup, Med. Phys. 39 (4) (2012).
[26] D.S. Taubman, M.W. Marcellin, JPEG 2000: Image Compression Fundamentals, Standards and Practice, Kluwer Academic Publishers, 2001.
[27] M. Unser, Sampling-50 years after Shannon, Proc. IEEE 88 (4) (2000) 569–587.
[28] D. Donoho, X. Huo, Uncertainty principles and ideal atomic decomposition, IEEE Trans. Inf. Theory 47 (7) (2001) 2845–2862.
[29] R. Coifman, F. Geshwind, Y. Meyer, Noiselets, Appl. Comput. Harmon. Anal. 10 (1) (2001) 27–44.
[30] M. Abramoff, P.J. Magalhães, S.J. Ram, Image processing with ImageJ, Biophotonics Int. 11 (7) (2004) 36–42.
[31] J. Bect, L. Blanc-Féraud, G. Aubert, A. Chambolle, A l1-Unified Variational Framework for Image Restoration, Springer Berlin Heidelberg, Berlin, Heidelberg, 2004.
[32] J.A. Tropp, S.J. Wright, Computational methods for sparse solution of linear inverse problems, Proc. IEEE 98 (6) (2010) 948–958.
[33] G.-H. Chen, J. Tang, S. Leng, Prior image constrained compressed sensing (PICCS): a method to accurately reconstruct dynamic CT images from highly undersampled projection data sets, Med. Phys. 35 (2) (2008) 660.
[34] J. Provost, F. Lesage, The application of compressed sensing for photo-acoustic tomography, IEEE Trans. Med. Imaging 28 (4) (2009) 585–594.
[35] K. Song, L.R. Comolli, M. Horowitz, Removing high contrast artifacts via digital inpainting in cryo-electron tomography: an application of compressed sensing, J. Struct. Biol. 178 (2) (2012) 108–120.
[36] A. Stoschek, R. Hegerl, Denoising of electron tomographic reconstructions using multiscale transformations, J. Struct. Biol. 120 (3) (1997) 257–265.
[37] C. Sorzano, E. Ortiz, M. López, J. Rodrigo, Improved Bayesian image denoising based on wavelets with applications to electron microscopy, Pattern Recognit. 39 (6) (2006) 1205–1213.
[38] C. Vonesch, L. Wang, Y. Shkolnisky, A. Singer, Fast wavelet-based single-particle reconstruction in Cryo-EM, in: 2011 IEEE Int. Symp. Biomed. Imaging From Nano to Macro, IEEE, 2011, pp. 1950–1953.
[39] R.A. Brooks, G.H. Weiss, A.J. Talbert, A new approach to interpolation in computed tomography, J. Comput. Assist Tomogr. 2.5 (2010) 577–585.
[40] M. Nilchian, C. Vonesch, P. Modregger, M. Stampanoni, M. Unser, Fast iterative reconstruction of differential phase contrast X-ray tomograms, Opt. Express 21 (5) (2013) 5511.
[41] F. Natterer, The Mathematics of Computerized Tomography, Society for Industrial and Applied Mathematics, 2001.
[42] U. Kamilov, E. Bostan, M. Unser, Wavelet shrinkage with consistent cycle spinning generalizes total variation denoising, IEEE Signal Process. Lett. 19 (4) (2012) 187–190.
[43] M. Unser, P.D. Tafti, An introduction to sparse stochastic processes, Cambridge University Press, 2014.
[44] E.J. Candes, J.K. Romberg, T. Tao, Stable signal recovery from incomplete and inaccurate measurements, Commun. Pure Appl. Math. 59 (8) (2006) 1207–1223.
[45] M. Persson, D. Bone, H. Elmqvist, Total variation norm for three-dimensional iterative reconstruction in limited view angle tomography, Phys. Med. Biol. 46 (3) (2001) 853.
[46] E.Y. Sidky, X. Pan, Image reconstruction in circular cone-beam computed tomography by constrained, total-variation minimization, Phys. Med. Biol. 53 (17) (2008) 4777.
[47] L. Ritschl, F. Bergner, C. Fleischmann, M. Kachelrieß, Improved total variation-based ct image reconstruction applied to clinical data, Phys. Med. Biol. 56 (6) (2011) 1545.
[48] S. Trepout, C. Messaoudi, S. Perrot, P. Bastin, S. Marco, Scanning transmission electron microscopy through-focal tilt-series on biological specimens., Micron 77 (2015) 9–15.
[49] M. Nilchian, J.P. Ward, C. Vonesch, M. Unser, Optimized kaiser-bessel window functions for computed tomography, IEEE Trans. Image Process. 24 (11) (2015) 3826–3833, doi:10.1109/TIP.2015.2451955.
[50] R. Brun, Schönenberger, Cultivation and in vitro cloning or procyclic culture forms of Trypanosoma brucei in a semi-defined medium. Short communication., Acta Trop. 36 (3) (1979) 289–292.
[51] W. Saxton, W. Baumeister, M. Hahn, Three-dimensional reconstruction of imperfect two-dimensional crystals, Ultramicroscopy 13 (1–2) (1984) 57–70.
[52] S. Ramani, J.A. Fessler, A splitting-based iterative algorithm for accelerated statistical X-Ray CT reconstruction, IEEE Trans. Med. Imaging 31 (3) (2012) 677–688.
[53] S. Boyd, N. Parikh, E. Chu, B. Peleato, J. Eckstein, Distributed optimization and statistical learning via the alternating direction method of multipliers, Found. Trends® Mach. Learn. 3 (1) (2010) 1–122.